APL Materials

RESEARCH ARTICLE | MAY 09 2023

High spin polarization and spin signal enhancement in non-local spin valves with Co–Fe alloy injectors and detectors

B. Kaiser ; J. Ramberger ; J. D. Watts ; J. Dewey ; Zhang Y. (張易) ; C. Leighton

APL Mater 11, 051108 (2023)
https://doi.org/10.1063/5.0147465

High spin polarization and spin signal enhancement in non-local spin valves with Co–Fe alloy injectors and detectors

Cite as: APL Mater. 11, 051108 (2023); doi: 10.1063/5.0147465
Submitted: 22 February 2023 • Accepted: 20 April 2023 •
Published Online: 9 May 2023

B. Kaiser, J. Ramberger, J. D. Watts, J. Dewey, Y. Zhang (張易), and C. Leighton[a)]

AFFILIATIONS

Department of Chemical Engineering and Materials Science, University of Minnesota, Minneapolis, Minnesota 55455, USA

[a)]Author to whom correspondence should be addressed: leighton@umn.edu

ABSTRACT

For applications such as spin accumulation sensors for next-generation hard disk drive read heads, and for fundamental research, it is desirable to increase the spin signal in metallic non-local spin valves, which are central devices in spintronics. To this end, here, we report on the integration of high-spin-polarization Co–Fe binary alloy ferromagnetic injectors and detectors in Al-based non-local spin valves. Room-temperature deposition on amorphous substrates from an alloy target is shown to generate smooth, polycrystalline (110-textured), solid-solution body-centered-cubic $Co_{75}Fe_{25}$ films, which we characterize by energy dispersive x-ray spectroscopy, x-ray diffraction, x-ray reflectivity, atomic force microscopy, and electronic transport. Simple integration into transparent-interface Al non-local spin valves is then shown to realize up to a factor of ~5 enhancement of the spin signal relative to Co, with full quantitative analysis yielding strikingly temperature-independent current spin polarizations exceeding 60%. We make a detailed quantitative comparison of these values with prior literature, concluding that Co–Fe alloys present a remarkably facile route to higher spin polarization and spin signals in non-local spin valves, with minimal barrier to adoption.

INTRODUCTION

The non-local spin valve (NLSV) is a central device in spintronics.[1–43] In essence, NLSVs enable the electrical injection of non-equilibrium spin polarization from a ferromagnet (F1) into a nonmagnetic (N) nanowire, coupled with non-local detection of the spin polarization that persists to a second ferromagnet (F2) at separation d.[5–43] Pure, diffusive spin currents are thus generated in the N "channel," providing a direct probe of spin transport in the N material. In particular, the non-local resistance change (ΔR_{NL}) when the ferromagnets are toggled between parallel and antiparallel magnetization can be measured vs d, directly determining the N material spin diffusion length, λ_N.[5–43] When combined with a local transport measurement of the resistivity (ρ_N) in the N channel (and thus the electron diffusivity), this additionally provides the lifetime of the injected spins, τ_s.[9–11] λ_N, τ_s, and their temperature (T) dependence are vital to the understanding of spin transport in N materials, and so NLSV-based analyses have been applied widely, including to metals,[5–11,17–43] semiconductors,[12–15] and two-dimensional materials.[16]

Metallic NLSVs have also been proposed as a next-generation read head technology for ultrahigh-density hard disk drives.[17–20] The essential concept in these "spin accumulation sensors" is to laterally couple a free F detector at the hard disk surface to a pinned F reference layer via a diffusive spin current through a metallic N film. This design, which is essentially a metallic NLSV, minimizes the read head footprint at the hard disk air bearing surface (only a thin F free layer and N film are needed), scales favorably with d and the F and N nanowire widths, could have favorable noise relative to other designs, and presents low resistance-area product (RA).[17–20] The latter is critical, as it provides a potential means to avoid the impedance mismatch problems due to high RA in the scaled magnetic tunnel junction (MTJ) read heads currently used in hard disk drives, thereby addressing a looming technological problem.[17–20] Controlled "tunnel" barriers at the F/N interfaces also provide a route to tune RA and optimize ΔR_{NL} by mitigating back

diffusion of spins (spin sinking) into the F electrodes.[21–24] Realization of such spin accumulation sensors, however, requires improved spin transport through ultrathin N metal films (as required for high-density recording) as well as improvements in the "spin signal" ΔR_{NL}.[17–20]

Enhancement of ΔR_{NL} in metallic NLSVs is thus not only of fundamental importance, where it can facilitate accurate measurement of spin injection and transport, but is also highly desirable technologically. Tunable *RA* barriers at the F/N interfaces are one means to enhance ΔR_{NL} and are being actively pursued,[21–24] as is the improvement of the spin polarization (α) of the F injectors/detectors. The latter is rooted in the rapid increase in ΔR_{NL} with α in metallic NLSVs, which follows $\Delta R_{NL} \propto \alpha^2/(1 - \alpha^2)$ in the limit of transparent F/N interfaces and $\Delta R_{NL} \propto \alpha^2$ in the tunneling limit.[44] Highly spin-polarized or half-metallic ferromagnets are thus being actively explored in metallic NLSVs, most notably Heusler alloys.[19,25–29] While this is clearly promising, it is also useful and practical to consider the integration of simpler high-polarization ferromagnets into NLSVs, particularly those that do not require specialized deposition techniques, atomic ordering, high-temperature deposition, post-deposition annealing, or other processing that might present integration challenges. In this sense, Co–Fe binary alloys and related systems (e.g., Co–Fe–B) are of high interest, especially given their outstanding performance in other spintronic devices such as MgO-based MTJs.[1–4,19,20] In $Co_{1-x}Fe_x$, for example, a maximum in polarization is thought to occur around $x \approx 0.25$ ($Co_{75}Fe_{25}$), potentially related to electronic structure changes associated with the transformation to body-centered-cubic (BCC),[45] generating α well above Co, Fe, $Ni_{80}Fe_{20}$, and so on.[30–34,46,47]

Significantly, while the integration of binary F alloys such as $Co_{1-x}Fe_x$ into metallic NLSVs has been reported,[30–35] the findings

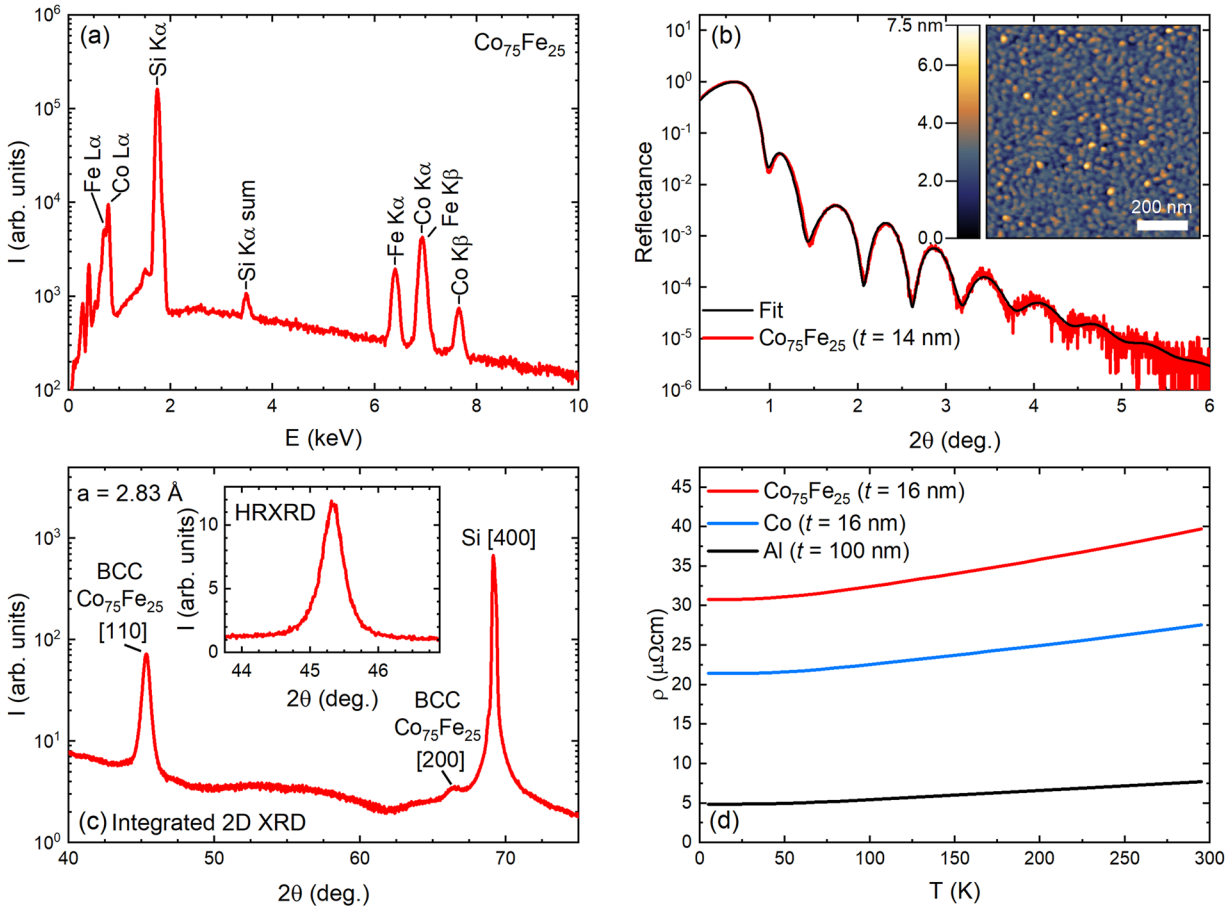

FIG. 1. (a) Energy-dispersive x-ray spectroscopy [EDS, intensity (I) vs energy, (E)] from a 100-nm-thick Co–Fe film grown from a $Co_{80}Fe_{20}$ source, with a 2-nm-thick Al cap layer. Analysis of the Co and Fe peaks (labeled) yields a composition of $Co_{75}Fe_{25}$. (b) Specular grazing-incidence x-ray reflectivity [GIXR, reflectance vs angle (2θ)] from a 14-nm-thick $Co_{75}Fe_{25}$ film (also with a 2-nm-thick Al cap layer) along with a GenX[49] fit. Inset: Atomic force micrograph (AFM) of the same film, resulting in 0.7 nm root-mean-square roughness and 25 nm in-plane grain size. (c) Wide-angle specular x-ray diffraction (XRD, I vs 2θ) from a 300-nm-thick $Co_{75}Fe_{25}$ film with substrate and film peaks labeled. These data were obtained by integration of two-dimensional-detector data (see the supplementary material, Fig. S1 for details). Inset: Specular high-resolution x-ray diffraction (HRXRD) around the 110 peaks, yielding lattice parameter $a = 2.83$ Å. (d) Resistivity (ρ) vs temperature (T) for $Co_{75}Fe_{25}$(16 nm), Co (16 nm), and Al(100 nm) nanowires.

are notably scattered. Spin polarizations between 20% and 58% have been reported, across various x, with significant spreads in F resistivity (ρ_F) and spin diffusion length (λ_F).[30–35] These values are also rarely accompanied by structural characterization,[30–32,34,35] typically do not report the $Co_{1-x}Fe_x$ crystal structure,[30–32,34,35] and often derive from NLSVs based on Cu channels,[30,32,35] where it is now known that the spin Kondo effect arising near the F/N interfaces can substantially suppress α from its true value.[9,10,36–41] The performance of Co–Fe F injectors/detectors in metallic NLSVs, and their usefulness for applications, is thus not entirely clear.

We address this situation here by reporting on the integration of $Co_{75}Fe_{25}$ thin-film F injectors/detectors in Al-based (i.e., Kondo-effect-free) all-metal NLSVs. Room-temperature deposition of $Co_{75}Fe_{25}$ from an alloy target onto amorphous substrates with no post-deposition annealing is shown to generate smooth, polycrystalline (110-textured), solid-solution BCC films, which we characterize via energy dispersive x-ray spectroscopy (EDS), x-ray diffraction (XRD), grazing-incidence x-ray reflectivity (GIXR), atomic force microscopy (AFM), and T-dependent transport measurements. Remarkably, these Co–Fe alloy ferromagnets generate up to a factor of ~5 enhancement of ΔR_{NL} relative to Co, with full quantitative analysis establishing that this is due to strikingly T-independent α that exceeds 60%, even at room temperature. We provide a detailed quantitative comparison of these values to prior reports, concluding that many apparent discrepancies stem simply from differences in device geometry and analysis approach, particularly with respect to λ_F. We thus argue that Co–Fe alloys present a facile route to higher α and ΔR_{NL} in non-local spin valves, with a very low barrier to adoption, and could be combined with tuning of the F/N interface RA in the future work to optimize ΔR_{NL} for applications.

EXPERIMENTAL DETAILS

To assess the merits of Co–Fe over standard elemental ferromagnets, multiple sets of all-metal NLSVs with Al channels were fabricated with both $Co_{75}Fe_{25}$ and Co injectors/detectors. A full description of fabrication methods is provided in the supplementary material, Sec. A, and has been reported before.[9–11,37–39,41,43] Briefly, electron beam lithography was first used to create shadow masks from bilayer resist films on Si/Si–N substrates. Multi-angle deposition, an established technique for NLSVs (see Refs. 7, 9–11, 38, 39, and 41–43), was then used for single-shot deposition of NLSVs, i.e., with no air exposure between the deposition of the F and N layers. This employed ultrahigh-vacuum electron-beam evaporation (base pressure ~ 10^{-11} Torr) of Al (from a 99.999% pure target at 0.5 Å s^{-1}), Co (99.95% pure, 0.5 Å s^{-1}), and $Co_{80}Fe_{20}$ (99.95% pure, 0.5 Å s^{-1}) onto room-temperature substrates, defining channel and injector/detector widths down to ~200 and ~100 nm, respectively. For NLSVs, the F and N thicknesses were fixed at 16 and 100 nm, respectively, although single $Co_{75}Fe_{25}$ films were characterized at various thicknesses. As emphasized below, electron beam evaporation from a $Co_{80}Fe_{20}$ target was found to repeatably and stably generate $Co_{75}Fe_{25}$ films, over many depositions. To facilitate direct comparison, pairs of Co and Co–Fe NLSVs were fabricated with Al channels from the exact same deposition. Multiple d values were also patterned on single wafers to enable the most reliable possible extraction of α and λ_N.

EDS, XRD, GIXR, and AFM employed JEOL JSM-6010PLUS/LA, Bruker D8 Discover, Rigaku Smartlab XE, and Bruker Nanoscope V Multimode 8 systems, respectively. Charge and spin transport measurements (5–300 K) were performed in a helium flow cryostat with a superconducting magnet using a Lakeshore 370 AC resistance bridge sourcing 316 μA at 13.7 Hz. The charge transport measurements consist of T-dependent measurements of the N and F resistivities ρ_N and ρ_F, while the spin transport measurements consist primarily of T-dependent measurements of the NLSV spin signal ΔR_{NL}.

RESULTS

Beginning with the characterization of single Co–Fe films, Fig. 1(a) shows a typical EDS result from a

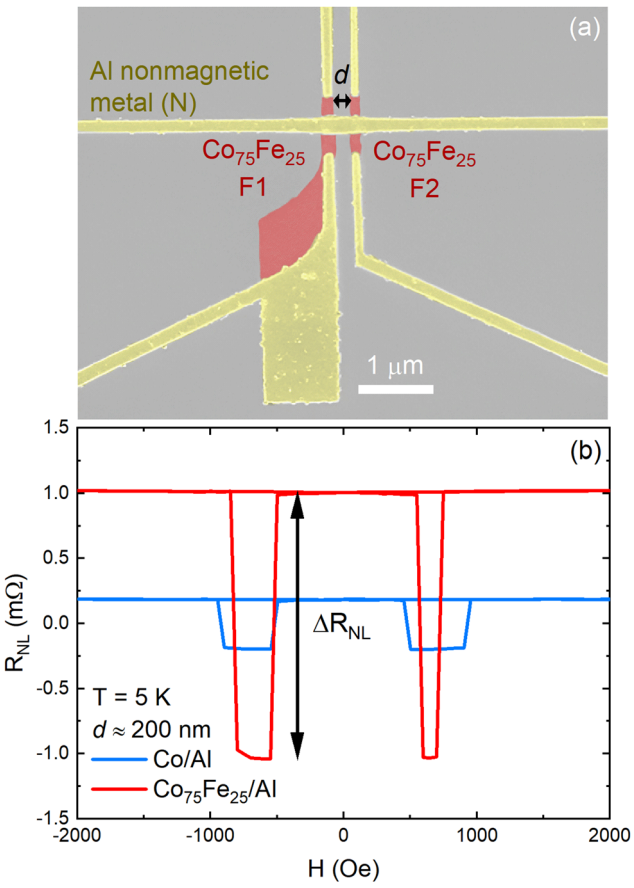

FIG. 2. (a) False-color scanning electron micrograph of an example $Co_{75}Fe_{25}$/Al-based NLSV, highlighting the nonmagnetic (N) channel, ferromagnetic (F) injector/detector, and separation d. The F injector/detector is designed with different widths (and a domain nucleation pad in one case) to facilitate distinct switching fields and thus a well-defined antiparallel state. (b) 5-K background-subtracted non-local resistance (R_{NL}) vs applied in-plane field (H) for $d \approx 200$ nm Al-based NLSVs with Co (blue) or $Co_{75}Fe_{25}$ (red) ferromagnetic injectors/detectors. As noted in the text, the field asymmetry results from exchange bias due to some oxidation of the Co–Fe layers; this does not impact ΔR_{NL}.

Si/Si–N/Co–Fe(100 nm)/Al(2 nm) sample. Aside from typical contamination peaks, only Si, Co, and Fe are detected, the extracted composition being $Co_{75}Fe_{25}$. The decrease in Co content from the target ($Co_{80}Fe_{20}$) is unsurprising (Fe has a slightly higher vapor pressure at the highest relevant temperatures[48]), and the modest magnitude of this decrease renders composition control simple. Moving on to GIXR, Fig. 1(b) shows reflectance vs angle (2θ) from a Si/Si–N/$Co_{75}Fe_{25}$(14 nm)/Al(2 nm) film along with a corresponding GenX[49] fit. Predominantly single-period Kiessig oscillations occur out to at least 5 degrees, with the fit yielding a Si–N/Co–Fe interface roughness of ~0.4 nm, a Co–Fe/Al interface roughness of ~0.8 nm, and $Co_{75}Fe_{25}$ density within 8% of bulk[50] (see the supplementary material, Table S1 for details). Low surface roughness was confirmed by PeakForce-QNM®-mode AFM on the same film [inset to Fig. 1(b)], which yielded 0.7 nm roughness and 25 nm in-plane grain size. Progressing to XRD, Fig. 1(c) displays an intensity vs 2θ plot. These data were obtained by integration of two-dimensional-detector data (see the supplementary material, Fig. S1 for details). Aside from the Si 400 peak, the main reflection is a BCC 110 Co–Fe peak, although a small additional BCC Co–Fe 200 peak is also visible, as confirmed by the two-dimensional patterns (Fig. S1). These data thus establish a simple BCC structure with no indications of atomic ordering at this $Co_{75}Fe_{25}$ composition. The strong (110) texture is then unsurprising as this is common in polycrystalline BCC metals, including on amorphous substrates.[51] The high-resolution scan in the inset to Fig. 1(c) focuses on the primary $Co_{1-x}Fe_x$ 110 reflection, yielding a lattice parameter of 2.83 Å, which is within 0.5% of reported values at similar x.[50]

A final piece of the Co–Fe film characterization is provided in Fig. 1(d), which shows $\rho(T)$ from a 16-nm-thick film patterned into a 300-nm-wide nanowire (i.e., similar width to our NLSVs), compared to the equivalent for Co. As expected for an atomically disordered alloy, the $Co_{75}Fe_{25}$ resistivity is substantially increased relative to Co, with the residual resistivity rising to 31 $\mu\Omega$ cm compared to 21 $\mu\Omega$ cm in Co. The overall picture from Fig. 1 is thus $Co_{75}Fe_{25}$ atomically disordered BCC films with strong (110) textures, nanoscale grains, and low surface roughness. These are desirable properties for NLSVs and are achieved here via simple room-temperature deposition from an alloy target with no post-deposition annealing.

Progressing to NLSVs, Fig. 2(a) presents a false-color scanning electron microscopy (SEM) image of a typical $Co_{75}Fe_{25}$/Al NLSV fabricated by the above methods (note that the 16-nm-thick F layer is deposited first, followed by the 100-nm-thick Al channel). In this device, d = 260 nm, and the F electrode widths are 140 and 90 nm. These differing F electrode widths facilitate distinct switching fields for the two Fs, as does the domain nucleation pad on the

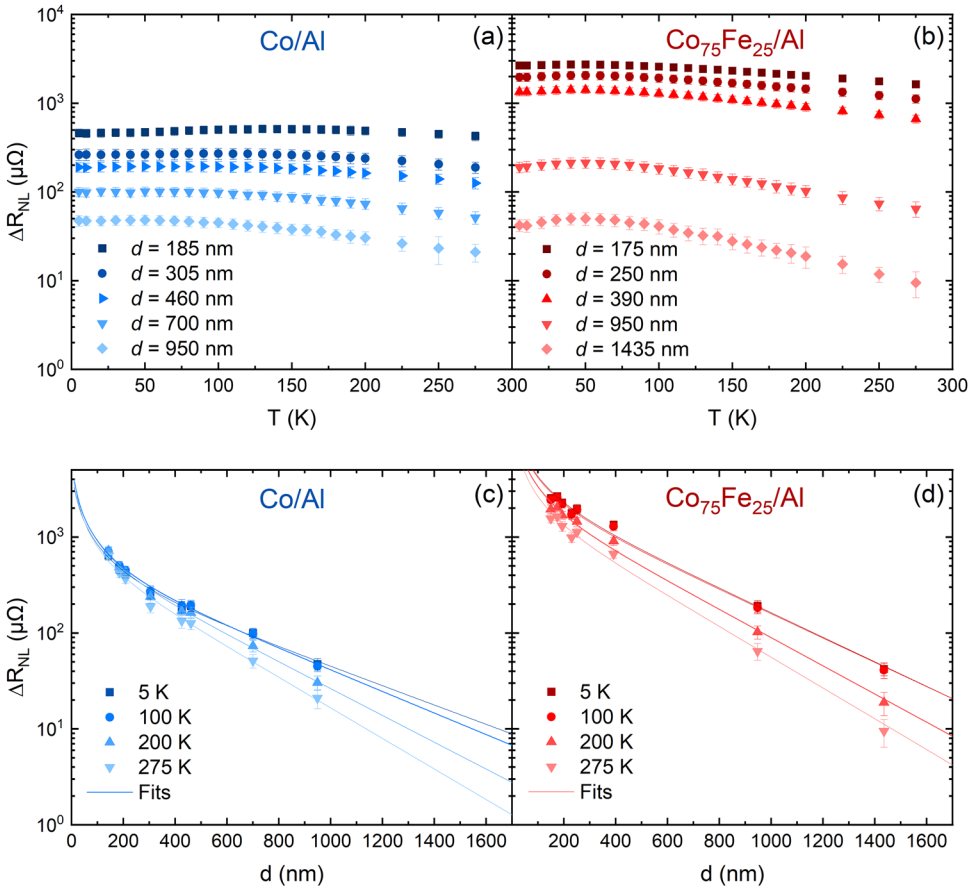

FIG. 3. Temperature (T) dependence of the non-local resistance change (ΔR_{NL}) (spin signal) for representative Al-based NLSVs based on (a) Co (blue) and (b) $Co_{75}Fe_{25}$ (red) at various injector-detector separations, d. (c) and (d) Temperature-dependent $\Delta R_{NL}(d)$ for the same devices shown in (a) and (b). Solid lines are fits to Eq. (1).[44] In the top and bottom panels, the darker/lighter shades of red and blue distinguish different d and T values.

wider F electrode[9] [which is visible in Fig. 2(a)], resulting in a well-defined antiparallel state. A key result from such devices is shown in Fig. 2(b), which plots the spin signal ΔR_{NL} vs in-plane magnetic field H, at $T = 5$ K and $d \approx 200$ nm, for both a Co/Al (blue) and an otherwise nominally identical $Co_{75}Fe_{25}$/Al (red) NLSV. The ΔR_{NL} in the $Co_{75}Fe_{25}$ case exceeds 2 mΩ [the double-ended arrow in Fig. 2(b)], in this transparent F/N interface device (i.e., one with no interfacial tunnel barrier), amounting to almost five times the typical Co/Al NLSV shown in Fig. 2(b). This immediately suggests substantial enhancement of α [because $\Delta R_{NL} \propto \alpha^2/(1-\alpha^2)$ in this transparent F–N interface case], a conclusion we rigorously quantify below. Note that the field asymmetry in the Co–Fe case in Fig. 2(b) simply results from some surface oxidation of the F layers, which is apparently (and unsurprisingly) stronger for Co–Fe than Co. This oxidation generates an antiferromagnetic oxide and thus some exchange bias,[52] which impacts the switching fields but not ΔR_{NL}.

A full comparison between $Co_{75}Fe_{25}$/Al (red, right panels) and Co/Al NLSVs (blue, left panels) is provided in Fig. 3, which presents $\Delta R_{NL}(T)$ at multiple d [Figs. 3(a) and 3(b)] as well as log-linear plots of $\Delta R_{NL}(d)$ at multiple T. Note again that these devices have Al channels fabricated in the same deposition. Figures 3(a) and 3(b) reveal that the enhancement in ΔR_{NL} for $Co_{75}Fe_{25}$ injectors/detectors over Co injectors/detectors is maintained at all d, with weak T dependence. As an aside, we note that the slight non-monotonicity in $\Delta R_{NL}(T)$ at low T is not due to the spin Kondo effect previously described by us[9,10,38,39,41] and others,[36,37,40] as this is known to be absent in Al channels[9,11] (this was in fact a primary motivation for our use of Al here). The slight non-monotonicity in $\Delta R_{NL}(T)$ may instead arise from differences between the exact forms of $\rho(T)$ for the N and F materials. A more quantitative comparison between Co- and CoFe-based NLSVs is enabled by Figs. 3(c) and 3(d), where the observed behavior of $\Delta R_{NL}(d)$ is characteristic of transparent (low RA) F/N interfaces in both the Co/Al and $Co_{75}Fe_{25}$/Al cases. Specifically, a rapid fall-off in ΔR_{NL} occurs at low d, followed by straight-line behavior on this log-linear plot at higher d, i.e., simple exponential decay controlled by λ_N. The deviation from pure exponential behavior at low d ($<\lambda_N$) is well-known in transparent-interface metallic NLSVs, arising due to the back-diffusion of injected spins into the F injectors, which act as spin sinks.[43,44]

Full quantitative analysis was performed by fitting the behavior in Figs. 3(c) and 3(d) to the standard formalism of Takahashi and Maekawa,[44] i.e., the transparent-interface-limit (which we have explicitly verified for our single-shot-deposited metallic NLSVs[9]) of the established one-dimensional NLSV model based on Valet–Fert theory.[53] This yields

$$\Delta R_{NL}(d,T) = 4\frac{\alpha^2 {R_F}^2}{\left(1-\alpha^2\right)^2 R_N}\frac{\exp\left(-d/\lambda_N\right)}{\left[1+\frac{2R_F}{(1-\alpha^2)R_N}\right]^2 - \exp\left(-2d/\lambda_N\right)}, \quad (1)$$

where α is now explicitly the current spin polarization, $R_N = \rho_N\lambda_N/w_N t_N$ and $R_F = \rho_F\lambda_F/w_N w_F$ are the spin resistances in the N and F, w_N and w_F are the N/F wire widths, and t_N is the N thickness. As detailed in our prior work, reliable extraction of $\lambda_N(T)$ and $\alpha(T)$ from data such as those in Figs. 3(c) and 3(d) using Eq. (1) requires significant care.[9–11,38,39,41,43] Here, we explicitly measured w_N and w_F in each device by SEM, determined $\rho_N(T)$ from local measurements on the same devices [see Fig. 1(d) for an example dataset], determined $\rho_F(T)$ from measurements of separate nanowire devices with similar width and identical thickness [also shown in Fig. 1(d)], and carefully constrained

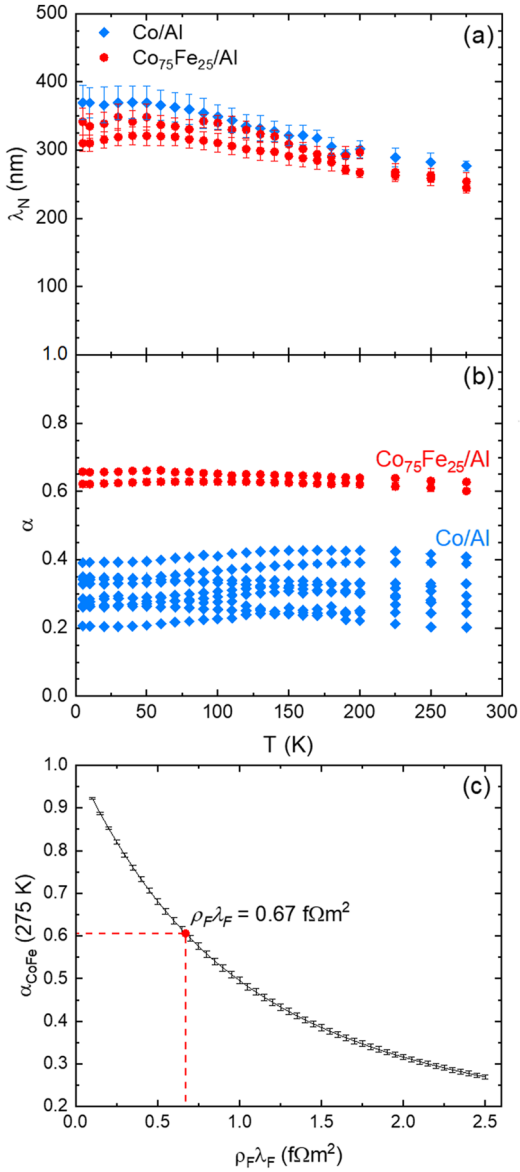

FIG. 4. Temperature (T) dependence of (a) the spin diffusion length (λ_N) and (b) the current spin polarization (α) from analysis of Al-based non-local spin valves with Co (blue) and $Co_{75}Fe_{25}$ (red) injectors/detectors. Two representative $Co_{75}Fe_{25}$ devices [the lower one is the device in Figs. 2(b), 3(b), and 3(d)] are compared to several Co devices. (c) Impact on the extracted α(275 K) value for $Co_{75}Fe_{25}$ of assuming different $\rho_F\lambda_F$ products, where ρ_F is the (measured) resistivity of the Co–Fe and λ_F is the (deduced) spin diffusion length of the Co–Fe. The red dashed lines depict the assumption used in this work, i.e., $\rho_F\lambda_F = 0.67$ fΩ m^2.[55] The error bars depict the uncertainty in the fitted α(275 K) value for a given $\rho_F\lambda_F$.

$\lambda_F(T)$.[9–11,38,39,41,43] We return to this in detail below, but the latter was achieved by using the previously established observation [from current-perpendicular-plane giant magnetoresistance (CPP GMR) measurements] that the $\rho_F\lambda_F$ product is constant for a given F.[54] For $Co_{70}Fe_{30}$, very close to our composition, $\rho_F\lambda_F$ = 0.67 fΩ m^2,[55] from which we can determine $\lambda_F(T)$ (as shown in Fig. S2) from our measured $\rho_F(T)$ [Fig. 1(d)]. An additional check on our fitting process was performed by comparing the extracted $\lambda_N(T)$ and $\alpha(T)$ from full fits to Eq. (1) at all d [solid lines in Figs. 3(c) and 3(d)] to values obtained by first determining $\lambda_N(T)$ uniquely from a simple exponential fit at high d and then using this to constrain the fit to Eq. (1).[9–11,38,39,41] [This is based on Eq. (1) simplifying to a single exponential at high d]. Reassuringly, these two approaches result in essentially identical $\lambda_N(T)$ and $\alpha(T)$.

The final resulting $\lambda_N(T)$ and $\alpha(T)$ are shown in Figs. 4(a) and 4(b) for two $Co_{75}Fe_{25}$/Al NLSVs and seven Co/Al NLSVs. As expected, the $\lambda_N(T)$ curves in Fig. 4(a) are rather similar for the $Co_{75}Fe_{25}$/Al and Co/Al devices. [They should be nominally identical in the absence of interfacial effects and indeed only minor differences are apparent in Fig. 4(a)]. λ_N rises from ~260 nm at room temperature to 310–340 nm at low temperature, which is qualitatively consistent with $\rho_N(T)$ [Fig. 1(d)]. Quantitatively, from these data, we estimate Elliott–Yafet constants (i.e., the proportionality constants between the spin and momentum relaxation times) for spin relaxation due to phonon scattering of 10 000–20 000. These are comparable to the 20 000 previously reported at ~100 nm thickness in an exhaustive study of Al spin transport.[11] More important in the current context, Fig. 4(b) shows that $\alpha(T)$ is distinctly different in $Co_{75}Fe_{25}$-based and Co-based devices. Consistent with prior reports,[11] seven example Co-based NLSVs (blue) in Fig. 4(b) exhibit some dispersion in the magnitude of α and its (weak) T dependence but with an average value of ~30%. In contrast, the α values in the two $Co_{75}Fe_{25}$/Al NLSVs in Fig. 4(b) (red) exceed 60%. The polarization in both devices also has notably weak T dependence (consistent with the high Curie temperature[56] and non-negligible magnetocrystalline anisotropy[57] at this $Co_{1-x}Fe_x$ composition), which is desirable from fundamental and applied perspectives. Current spin polarizations of up to more than 60% thus persist to room temperature, the approximate doubling with respect to the average Co/Al values underpinning the almost five-fold enhancement in ΔR_{NL} in Fig. 2(b).

DISCUSSION

It is important to properly place the above conclusions in the context of prior work on Co–Fe alloys. We first note that our ~62% spin polarization compares reasonably well with prior reports of 52% and 58% for similar compositions, from superconducting tunneling spectroscopy[46] and point contact Andreev reflection,[47] respectively. The Andreev result, which is closest to our value, is most directly comparable here due to its non-tunneling nature. Compared to prior Co–Fe-based metallic NLSV work, the situation becomes slightly more complicated. As noted above, some Co–Fe NLSV reports are based solely on Cu channels[30,32] (which are now understood to be subject to suppressed α due to Kondo effects near the F/N interfaces[9,10,36–41]), few report the $Co_{1-x}Fe_x$ crystal structure,[33] the chosen x value varies,[30–34] and the d range used to extract α and λ_N can be limited, in some cases to a single d value.[33] We thus mostly focus our comparisons here to the literature on Al-channel devices, with similar Co–Fe composition to our $Co_{75}Fe_{25}$, studied over substantial d ranges [thus enabling accurate determination of $\alpha(T)$ and $\lambda_N(T)$].[31,34]

The next challenge with respect to quantitative comparisons is that, as is clear from a close inspection of Eq. (1), and alluded to above, standard analyses of NLSVs do not enable separate determination of α and λ_F. Rather, extraction of α from $\Delta R_{NL}(d)$ data requires that λ_F is pinned down by some other means, typically from CPP GMR.[54] In our case, we do this based on CPP GMR data on the very close $Co_{70}Fe_{30}$ composition, which yielded $\rho_F\lambda_F$ = 0.67 fΩ m^2, independent of T,[55] enabling us to fix $\lambda_F(T)$ (see Fig. S2) from our measured $\rho_F(T)$. We consider this approach distinctly preferable to simply fixing λ_F at a constant value based on prior measurements, with no regard for the measured ρ_F.[33,34] This is particularly true when one considers from Eq. (1) that it is the product $\rho_F\lambda_F$ (which enters through R_F) that is convoluted with α. As can be seen from Fig. S2, the $\alpha(T)$ data in Fig. 4(a) are thus based on estimated $\lambda_F(T)$ values of ~2 nm. The impact of using other values of the $\rho_F\lambda_F$ product on the α values extracted from the data in Figs. 3(b) and 3(d) are shown in Fig. 4(c), using 275 K as an illustrative temperature. Assuming higher $\rho_F\lambda_F$ products than our chosen 0.67 fΩ m^2, setting λ_F at much higher values than our ~2 nm,[31,33,34] or using measured λ_F values (e.g., from spin absorption devices) larger than our ~2 nm,[30,32] decreases the determined α, reconciling apparent discrepancies with several prior works. Examples of the latter would be the lower 48% spin polarization for $Co_{60}Fe_{40}$ determined based on a measured λ_F of 6.2 nm (corresponding to $\rho_F\lambda_F$ = 1.24 fΩ m^2),[30] or the even lower 45% spin polarization for $Co_{84}Fe_{16}$ determined based on fixing λ_F at 11 nm (corresponding to $\rho_F\lambda_F$ = 2.53 fΩ m^2).[34] Particularly after accounting for differences in the definition of d (edge-to-edge vs center-to-center), these literature results fall into even quantitative agreement with Fig. 4(c).

The most direct literature comparison we can make turns out to be with the work of Zahnd *et al.*, who studied $Co_{60}Fe_{40}$ NLSVs with Al channels, a wide d range, demonstrated transparent F/N interfaces, and a similar $\rho_F\lambda_F$ to ours (0.98 fΩ m^2).[31] The result is a 300-K spin polarization of 58%,[31] close to our own ~62%, and, again, close to the Andreev reflection value of 58%.[47] We consider this strong confirmation that the true current spin polarization in $Co_{1-x}Fe_x$-based metallic NLSVs lies near 60%, even at room temperature. Finally, we note that the significantly larger ΔR_{NL} values reported for Co–Fe/Al NLSVs by Zahnd *et al.*[31] are mostly due to geometrical factors, particularly their smaller w_N (50 vs 200 nm), w_F (50 vs 100 nm), and d [150 vs 200 nm in Fig. 2(b)], as well as the larger λ_N (550 nm, due to their lower ρ_N). Accounting for these factors based on Eq. (1) in fact reconciles the magnitudes of ΔR_{NL} in the two works to within a factor of ~1.7, within the range of what minor changes in effective F/N contact area can easily explain.

The above findings, which confirm high spin polarization and spin signal in Co–Fe-based NLSVs, have significant implications for both fundamental spintronics research and potential applications. From the fundamental perspective, this work demonstrates that Co–Fe alloys can be straightforwardly integrated into NLSVs, achieving improved signal-to-noise ratio in $\Delta R_{NL}(T,d)$, the Hanle effect (i.e., perpendicular-field-induced spin decoherence measurements[9,38]), and so on, and thus simpler, more accurate,

more precise measurements of λ_N and τ_s. While established here for a typical metallic N (Al), similar gains would be expected for other N materials. From the applied point of view, future work could establish this type of metallic NLSV performance enhancement as a function of the F/N interface *RA* via, for example, controlled oxidation of an oxide tunnel barrier;[21,24] this would be an important step toward thorough optimization of ΔR_{NL} for spin accumulation sensors.

SUMMARY

We have demonstrated facile integration of binary alloy Co–Fe ferromagnetic injectors and detectors into Al-based non-local spin valves. Room-temperature deposition on amorphous substrates from an alloy target was shown to generate atomically disordered body-centered-cubic $Co_{75}Fe_{25}$ films, with strong (110) texture, nanoscale grains, and low surface roughness, with no need for post-deposition annealing. Full quantitative analysis of non-local spin valve data vs temperature and injector/detector separation revealed up to a factor of ~5 enhancement in spin signal relative to Co, due to current spin polarizations exceeding 60%, with very weak temperature dependence. This performance was compared to, and reconciled with, prior reports on $Co_{1-x}Fe_x$-based metallic non-local spin valves, leading to the conclusion that Co–Fe alloy ferromagnets provide a remarkably simple route to the enhancement of the spin signal and spin polarization, with minimal barrier to adoption.

SUPPLEMENTARY MATERIAL

See the supplementary material for additional x-ray reflectivity analysis, x-ray diffraction data, and determined Co–Fe spin diffusion lengths.

ACKNOWLEDGMENTS

This work was supported by the ASRC (Advanced Storage Research Committee) with additional support from the National Science Foundation through Grant No. DMR-2103711. Parts of this work were conducted in the Minnesota Nano Center, which is supported by the NSF through the National Nanotechnology Coordinated Infrastructure under Grant No. ECCS2025124, and in the UMN Characterization Facility, which is partially supported by the NSF through the MRSEC program. We acknowledge P. Crowell for useful comments and discussions and M. Manno for assistance with EDS analysis.

AUTHOR DECLARATIONS

Conflict of Interest

The authors have no conflicts to disclose.

Author Contributions

C.L. conceived of the study. B.K., J.R., J.D.W., J.D., and Y.Z. performed the fabrication, structural and chemical characterization, and electronic and spin transport measurements, under the guidance of C.L. Data analysis was spearheaded by B.K. and C.L. The paper was written by C.L. and B.K. with input from all authors.

B. Kaiser: Conceptualization (equal); Data curation (lead); Formal analysis (lead); Investigation (lead); Methodology (lead); Visualization (lead); Writing – original draft (equal); Writing – review & editing (equal). **J. Ramberger**: Formal analysis (supporting); Investigation (equal); Methodology (equal); Visualization (supporting); Writing – review & editing (supporting). **J.D. Watts**: Formal analysis (supporting); Investigation (supporting); Methodology (supporting); Writing – review & editing (supporting). **J. Dewey**: Formal analysis (supporting); Investigation (supporting); Methodology (supporting); Visualization (supporting); Writing – review & editing (supporting). **Y. Zhang**: Investigation (supporting); Methodology (supporting); Writing – review & editing (supporting). **C. Leighton**: Conceptualization (lead); Formal analysis (equal); Funding acquisition (lead); Investigation (equal); Methodology (equal); Project administration (lead); Resources (lead); Supervision (lead); Visualization (supporting); Writing – original draft (lead); Writing – review & editing (equal).

DATA AVAILABILITY

The data that support the findings of this study are available within the article and its supplementary material and are available from the corresponding author upon reasonable request.

REFERENCES

[1] I. Žutić, J. Fabian, and S. das Sarma, Rev. Mod. Phys. **76**, 323 (2004).
[2] F. Hellman, A. Hoffmann, Y. Tserkovnyak, G. S. D. Beach, E. E. Fullerton, C. Leighton, A. H. MacDonald, D. C. Ralph, D. A. Arena, H. A. Dürr, P. Fischer, J. Grollier, J. P. Heremans, T. Jungwirth, A. V. Kimel, B. Koopmans, I. N. Krivorotov, S. J. May, A. K. Petford-Long, J. M. Rondinelli, N. Samarth, I. K. Schuller, A. N. Slavin, M. D. Stiles, O. Tchernyshyov, A. Thiaville, and B. L. Zink, Rev. Mod. Phys. **89**, 025006 (2017).
[3] S. Maekawa, S. O. Valenzuela, E. Saitoh, and T. Kimura, *Spin Current* (Oxford University Press, Oxford, 2017).
[4] E. Y. Tsymbal and I. Žutić, *Handbook of Spin Transport and Magnetism* (CRC Press, New York, 2016).
[5] M. Johnson and R. H. Silsbee, Phys. Rev. Lett. **55**, 1790 (1985).
[6] F. J. Jedema, A. T. Filip, and B. J. van Wees, Nature **410**, 345 (2001).
[7] Y. Ji, A. Hoffmann, J. S. Jiang, and S. D. Bader, Appl. Phys. Lett. **85**, 6218 (2004).
[8] F. Casanova, A. Sharoni, M. Erekhinsky, and I. K. Schuller, Phys. Rev. B **79**, 184415 (2009).
[9] L. O'Brien, M. Erickson, D. Spivak, H. Ambaye, R. J. Goyette, V. Lauter, P. A. Crowell, and C. Leighton, Nat. Commun. **5**, 3927 (2014).
[10] J. D. Watts, L. O'Brien, J. S. Jeong, K. A. Mkhoyan, P. A. Crowell, and C. Leighton, Phys. Rev. Mater. **3**, 124409 (2019).
[11] J. D. Watts, J. T. Batley, N. A. Rabideau, J. P. Hoch, L. O'Brien, P. A. Crowell, and C. Leighton, Phys. Rev. Lett. **128**, 207201 (2022).
[12] A. T. Filip, B. H. Hoving, F. J. Jedema, B. J. van Wees, B. Dutta, and S. Borghs, Phys. Rev. B **62**, 9996 (2000).
[13] I. Appelbaum, B. Huang, and D. J. Monsma, Nature **447**, 295 (2007).
[14] X. Lou, C. Adelmann, S. A. Crooker, E. S. Garlid, J. Zhang, K. S. M. Reddy, S. D. Flexner, C. J. Palmstrøm, and P. A. Crowell, Nat. Phys. **3**, 197 (2007).
[15] J. M. Kikkawa and D. D. Awschalom, Nature **397**, 139 (1999).
[16] E. C. Ahn, npj 2D Mater. Appl. **4**, 17 (2020).

[17]M. Takagishi, K. Yamada, H. Iwasaki, H. N. Fuke, and S. Hashimoto, IEEE Trans. Magn. **46**, 2086 (2010).
[18]M. Yamada, D. Sato, N. Yoshida, M. Sato, K. Meguro, and S. Ogawa, IEEE Trans. Magn. **49**, 713 (2013).
[19]T. Nakatani, Z. Gao, and K. Hono, MRS Bull. **43**, 106 (2018).
[20]G. Albuquerque, S. Hernandez, M. T. Kief, D. Mauri, and L. Wang, IEEE Trans. Magn. **58**, 1 (2022).
[21]A. Vogel, J. Wulfhorst, and G. Meier, Appl. Phys. Lett. **94**, 122510 (2009).
[22]Y. Fukuma, L. Wang, H. Idzuchi, and Y. Otani, Appl. Phys. Lett. **97**, 012507 (2010).
[23]A. Spiesser, H. Saito, S. Yuasa, and R. Jansen, Phys. Rev. B **99**, 224427 (2019).
[24]S. O. Valenzuela and M. Tinkham, Appl. Phys. Lett. **85**, 5914 (2004).
[25]S. Wurmehl, P. J. Jacobs, J. T. Kohlhepp, H. J. M. Swagten, B. Koopmans, S. Maat, M. J. Carey, and J. R. Childress, Appl. Phys. Lett. **98**, 012506 (2011).
[26]Y. K. Takahashi, S. Kasai, S. Hirayama, S. Mitani, and K. Hono, Appl. Phys. Lett. **100**, 052405 (2012).
[27]K. Hamaya, N. Hashimoto, S. Oki, S. Yamada, M. Miyao, and T. Kimura, Phys. Rev. B **85**, 100404 (2012).
[28]K. Kasahara, Y. Fujita, S. Yamada, K. Sawano, M. Miyao, and K. Hamaya, Appl. Phys. Exp. **7**, 033002 (2014).
[29]S. Shirotori, S. Hashimoto, M. Takagishi, Y. Kamiguchi, and H. Iwasaki, Appl. Phys. Exp. **8**, 023103 (2015).
[30]G. Zahnd, L. Vila, V. T. Pham, M. Cosset-Cheneau, W. Lim, A. Brenac, P. Laczkowski, A. Marty, and J. P. Attané, Phys. Rev. B **98**, 174414 (2018).
[31]G. Zahnd, L. Vila, T. v. Pham, A. Marty, P. Laczkowski, W. Savero Torres, C. Beigné, C. Vergnaud, M. Jamet, and J.-P. Attané, Nanotechnology **27**, 035201 (2015).
[32]M. Cosset-Chéneau, L. Vila, G. Zahnd, D. Gusakova, V. T. Pham, C. Grèzes, X. Waintal, A. Marty, H. Jaffrès, and J. P. Attané, Phys. Rev. Lett. **126**, 027201 (2021).
[33]S. Oki, S. Yamada, N. Hashimoto, M. Miyao, T. Kimura, and K. Hamaya, Appl. Phys. Exp. **5**, 063004 (2012).
[34]G. Bridoux, M. v. Costache, J. van de Vondel, I. Neumann, and S. O. Valenzuela, Appl. Phys. Lett. **99**, 102107 (2011).
[35]A. Pfeiffer, R. M. Reeve, K. Elphick, A. Hirohata, and M. Kläui, Phys. Rev. Res. **3**, 023110 (2021).
[36]J. T. Batley, M. C. Rosamond, M. Ali, E. H. Linfield, G. Burnell, and B. J. Hickey, Phys. Rev. B **92**, 220420 (2015).
[37]K.-W. Kim, L. O'Brien, P. A. Crowell, C. Leighton, and M. D. Stiles, Phys. Rev. B **95**, 104404 (2017).
[38]L. O'Brien, D. Spivak, J. S. Jeong, K. A. Mkhoyan, P. A. Crowell, and C. Leighton, Phys. Rev. B **93**, 014413 (2016).
[39]J. D. Watts, J. S. Jeong, L. O'Brien, K. A. Mkhoyan, P. A. Crowell, and C. Leighton, Appl. Phys. Lett. **110**, 222407 (2017).
[40]X. Shen and Y. Ji, Phys. Rev. B **104**, 085101 (2021).
[41]A. J. Wright, M. J. Erickson, D. Bromley, P. A. Crowell, C. Leighton, and L. O'Brien, Phys. Rev. B **104**, 014423 (2021).
[42]M. V. Costache, G. Bridoux, I. Neumann, and S. O. Valenzuela, J. Vac. Sci. Technol. B **30**, 04E105 (2012).
[43]L. O'Brien, D. Spivak, N. Krueger, T. A. Peterson, M. Erickson, B. Bolon, C. C. Geppert, C. Leighton, and P. A. Crowell, Phys. Rev. B **94**, 094431 (2016).
[44]S. Takahashi and S. Maekawa, Phys. Rev. B **67**, 052409 (2003).
[45]J. Joshua Yang, A. K. Bengtson, C.-X. Ji, D. Morgan, and Y. A. Chang, Acta Mater. **56**, 1491 (2008).
[46]D. J. Monsma and S. S. P. Parkin, Appl. Phys. Lett. **77**, 720 (2000).
[47]S. V. Karthik, T. M. Nakatani, A. Rajanikanth, Y. K. Takahashi, and K. Hono, J. Appl. Phys. **105**, 07C916 (2009).
[48]R. E. Honig and D. A. Kramer, RCA Rev. **30**, 285 (1969).
[49]A. Glavic and M. Björck, J. Appl. Crystallogr. **55**, 1063 (2022).
[50]K. H. J. Buschow, P. G. van Engen, and R. Jongebreur, J. Magn. Magn. Mater. **38**, 1 (1983).
[51]J. M. E. Harper, K. P. Rodbell, E. G. Colgan, and R. H. Hammond, J. Appl. Phys. **82**, 4319 (1997).
[52]B. L. Le, D. W. Rench, R. Misra, L. O'Brien, C. Leighton, N. Samarth, and P. Schiffer, New J. Phys. **17**, 023047 (2015).
[53]T. Valet and A. Fert, Phys. Rev. B **48**, 7099 (1993).
[54]J. Bass and W. P. Pratt, J. Phys.: Condens. Matter Phys. **19**, 183201 (2007).
[55]C. Ahn, K.-H. Shin, R. Loloee, J. Bass, and W. P. Pratt, J. Appl. Phys. **108**, 023908 (2010).
[56]A. S. Normanton, P. E. Bloomfield, F. R. Sale, and B. B. Argent, Metal Sci. **9**, 510 (1975).
[57]R. C. O'Handley, *Modern Magnetic Materials* (Wiley, Hoboken, 1999), p. 375.